Helicase-mediated mechanism of SSU processome maturation and disassembly

Olga Buzovetsky[1] and Sebastian Klinge[1,*]

1 Laboratory of Protein and Nucleic Acid Chemistry, The Rockefeller University, New York, New York 10065, USA

*Correspondence: klinge@rockefeller.edu (S.K.)

SUMMARY

Eukaryotic ribosomal small subunit (SSU) assembly requires the SSU processome, a nucleolar precursor containing the RNA chaperone U3 snoRNA. The underlying molecular mechanisms of SSU processome maturation, remodeling, disassembly, RNA quality control, and the transitions between states remain elusive due to a paucity of intermediates[1–3]. Here we report 16 native SSU processome structures alongside genetic data, revealing how two helicases, the Mtr4-exosome and Dhr1, are controlled for accurate and unidirectional ribosome biogenesis. Our data show how irreversible pre-ribosomal RNA degradation by the redundantly tethered RNA exosome couples the transformation of the SSU processome into a pre-40*S* particle during which Utp14 can probe evolving surfaces, ultimately positioning and activating Dhr1 to unwind the U3 snoRNA and initiate nucleolar pre-40*S* release. This study highlights a paradigm for large dynamic RNA-protein complexes where irreversible RNA degradation drives compositional changes and communicates these changes to govern enzyme activity while maintaining overall quality control.

47 **MAIN**

48 The nucleolus, a membrane-less organelle, is generated via eukaryotic ribosome
49 biogenesis in a transcription-dependent manner. The maturation of ribosomal small
50 subunit (SSU) and large subunit (LSU) precursors generates distinct phases of this multi-
51 layered organelle, which is maintained via multi-valent RNA-protein and protein-protein
52 interactions. Early stages of eukaryotic ribosomal small subunit (SSU/40*S*) assembly
53 involve the SSU processome, a giant nucleolar particle containing approximately a
54 quarter of all eukaryotic ribosome assembly factors and three RNAs (SSU pre-rRNA/18*S*,
55 a 5′ external transcribed spacer (5′ ETS) and the RNA chaperone U3 snoRNA)[1–3]. The
56 18*S* is composed of four domains (5′, central, 3′ major, and 3′ minor) which are housed
57 in separate modules. By serving as the architectural blueprint for the SSU processome,
58 the chaperone U3 snoRNA base-pairs with parts of the SSU pre-rRNA (via its box A and
59 box A' segments) as well as the 5′ ETS (via its 3' and 5' hinges). High-resolution structural
60 studies of SSU processome assembly and maturation in yeast and human cells have
61 started to reveal isolated native states before and after cleavage of the mature rRNA 5′
62 end (site A1) [4–13]. After a poorly characterized departure of most assembly factors (SSU
63 processome disassembly) a pre-40*S* particle emerges, which in addition to compacted
64 rRNA domains still contains U3 snoRNA and the RNA helicase Dhr1[ref9] . The current
65 absence of intermediate states highlights our limited understanding of the mechanisms
66 that guide transitions between visualized states. The transition of the SSU processome
67 from maturation to disassembly was suggested to involve the RNA exosome (with
68 associated exonuclease Rrp6 and RNA helicase Mtr4)[10,12–15]. As the arbiter of RNA
69 quality control, the RNA exosome ensures correct RNA processing with Rrp6 acting as

70 an initial distributive RNA exonuclease before more processive RNA degradation by
71 Rrp44. This system requires synergistic interactions between the RNA exosome and its
72 substrates for RNA surveillance. Substrates that remain tethered to the RNA exosome
73 are subject to RNA turnover whereas correctly processed RNA substrates are released[16].
74 The limited number of visualized SSU processome maturation and disassembly states
75 has prevented a mechanistic understanding of their interaction with the RNA exosome
76 and how RNA exosome function is coupled to SSU processome maturation and
77 disassembly. Specifically, the mechanisms of RNA exosome recruitment, substrate
78 access, and disengagement remain unclear[12,13].

79 At the end of SSU processome disassembly, the DEAH-box helicase Dhr1 (DHX37
80 in humans) plays a key role in the removal of U3 snoRNA from a pre-40*S* particle to
81 facilitate the formation of the central pseudoknot. However, despite ample studies[17–21],
82 the mechanism with which Dhr1 is initially recruited to the SSU processome, kept in an
83 inactive conformation, subsequently repositioned to engage its substrate U3 snoRNA,
84 and ultimately activated, remains unknown. Presently there is a lack of understanding of
85 how the SSU processome, the RNA exosome, and Dhr1 work in concert to bring about
86 unidirectional maturation and disassembly while maintaining RNA quality control
87 throughout the entire process, which enables completed particles to leave from the
88 nucleolus.

89 To address this, we determined native high-resolution structures of 16
90 *Saccharomyces cerevisiae* SSU processome states undergoing maturation and
91 disassembly with resolutions up to 2.7 Ångstroms. Together with complementary genetics
92 and an *in silico* protein-protein interaction screen, we have elucidated an RNA exosome-

93 mediated mechanism that explains both SSU processome maturation and disassembly
94 as a function of the 3′ to 5′ helicase activity of the RNA exosome-bound helicase Mtr4.
95 Within this framework SSU processome disassembly, exosome-mediated RNA
96 surveillance, and Dhr1 activation are tightly coordinated to maintain RNA quality control
97 during the entire pathway.

98 To determine how Dhr1-bound SSU processomes undergo maturation and
99 disassembly, we obtained native cryo-EM structures of particles containing Dhr1 during
100 early, intermediate, and late stages (**Fig. 1 and Extended Data Fig. 1**). Early assembly
101 states were selected using Dhr1 and the early assembly factor Kre33 as affinity baits
102 (Dataset 1, **Supplementary Fig. 1**). For unbiased views of all Dhr1-bound states, Dhr1
103 was used as the sole affinity bait (Dataset 2, **Supplementary Fig. 2**). The late
104 disassembly state containing activated Dhr1 (here State O) was obtained by selecting for
105 particles containing Dhr1 and its activator Utp14 and lacking Utp7, which is present in
106 earlier intermediates (Dataset 3, **Supplementary Fig. 3**).

107 From a total of 213,766 cryo-EM images, initial data curation and comprehensive
108 3D classifications yielded 16 SSU processome reconstructions (states A-O) with overall
109 resolutions of 2.7-6 Ångstroms (**Fig. 1 and Extended Fig. 1**). Focused refinements with
110 105 maps were used to obtain 16 composite maps for all structures (**Supplementary**
111 **Figs. 4-25**), which enabled model building and assignment of 50 unique assembly factors,
112 21 ribosomal proteins, and three RNAs (5′ ETS, 18S rRNA, and U3 snoRNA) across all
113 states (**Supplementary Tables 1 & 2**). Here, states are defined based on distinct rRNA
114 folding transitions and the presence or absence of distinct assembly factors resulting in
115 15 unique states (States A-O), and a substate of State A that undergoes conformational

116 changes only (State A*). Together these states provide unprecedented high-resolution
117 coverage of native SSU processome maturation and disassembly that goes far beyond
118 prior studies[9,10,12] (**Extended Data Fig. 1-6, Supplementary Fig. 26 and 27**). High-
119 resolution reconstructions further reveal the positions of post-translational modifications
120 and their role in stabilizing distinct assembly intermediates (**Supplementary Fig. 28**)
121

122 **Chronology of SSU biogenesis**

123 The large number of observed states allows us to visualize nucleolar SSU biogenesis as
124 a function of RNA exosome-mediated 5′ ETS degradation, which first triggers cleavage
125 of the 18*S* rRNA at site A1 (States A-G), and subsequently orchestrates SSU processome
126 disassembly, rRNA compaction, and activation of Dhr1 (States H-O) (**Fig. 1, Extended**
127 **Data Fig. 1 and 2**). The presence of the Rrp6 C-terminus in States C-L highlights the
128 tethered presence of the RNA exosome, which is mediating transitions between states.
129 This is contrary to prior studies which lacked the temporal resolution to precisely define
130 both the chronology and causality of events leading to cleavage at site A1 and hence the
131 underlying mechanism (**Supplementary Fig. 26**)[9]. Initial degradation of the 3′ end of the
132 5′ ETS on the exterior of the particle is followed by accommodation of the C-terminus of
133 Rrp6 (State C), suggesting that the RNA exosome is responsible for this remodeling step.
134 In State D the restructuring of the 5′ ETS in the interior of the SSU processome allows for
135 partial release of Krr1 and Faf1 from their binding sites. This leads to the 3′ end of the
136 18*S* rRNA precursor (helix 45) being chaperoned by the assembly factor Pno1 towards
137 the interior of the particle, thus allowing an N-terminal element of the DEAH-box helicase
138 Dhr1 to bind. As the assembly factor Utp14 connects Pno1 with Dhr1 (**Supplementary**

139 **Fig. 27 e and i**), the integration of helix 45 near the central domain results in the docking
140 of the auto-inhibited Dhr1 in State E. Surprisingly we find that A1 cleavage in State G is
141 solely triggered by the incorporation of Dim1. Here Dim1 probes the placement of helix
142 45 close to the central domain and stabilizes U3 snoRNA-bound regions of the 18S rRNA
143 in an upward conformation. This facilitates Utp24-mediated A1 cleavage in particles that
144 still contain the Kre33 module, which was previously thought to precede A1
145 cleavage[9] (**Fig. 1, Extended Data Fig. 3**).

146 SSU processome disassembly further progresses as a function of 3′ to 5′
147 elimination of the 5′ ETS, resulting in compositional and conformational changes of the
148 particle (**Fig.1**). During these compositional changes, Utp14, a largely unstructured
149 protein containing several regulatory segments visualized in our structures (here referred
150 to as a-f) can adopt different binding conformations as a response to SSU processome
151 maturation and disassembly (**Extended Data Fig.6 a,d,e**).

152 With the processing of the 5′ hinge, distinct stages of disassembly are observed
153 that involve the stepwise departure of assembly factors, such as Rrp5, Sof1, and Utp7
154 (States H-J). In States J and K, Utp14 licenses a new binding site for Dhr1, which was
155 previously occupied by Utp7. The subsequent processing of the 3′ hinge (States K-L)
156 releases much of the UtpB complex (except for Utp18) and the helicase Dhr1. In a major
157 compositional remodeling step, the transition from State L to M marks the complete
158 elimination of the 5′ ETS, which triggers the departure of the UtpA and UtpB complexes
159 as well as individual assembly factors and Rrp6. This remodeling step subsequently
160 allows Dhr1 to be repositioned and activated by Utp14 in a state-specific manner. States
161 M-O therefore capture the activation of Dhr1 as further compaction of the particle triggers

162 the undocking of U3 snoRNP proteins and Utp20. These results suggest a direct
163 mechanism by which the RNA exosome could degrade the 5′ ETS to trigger large
164 compositional and conformational changes that transform the SSU processome into a
165 pre-40*S* particle.
166
167 **Integrated nucleolar RNA surveillance**
168 Genetic studies suggested that the yeast RNA exosome binds the SSU processome via
169 an interaction between the RNA helicase Mtr4 arch domain and the assembly factor
170 Utp18 via an arch-interacting motif (AIM)[14] . While low-resolution density for the RNA
171 exosome in the proximity of the SSU processome has been observed[10,12], exactly how
172 exosome recruitment and positioning is achieved across multiple states remains unclear.
173 Moreover, the RNA exosome must efficiently detect and eliminate trapped SSU
174 precursors within the nucleolus which have failed to complete biogenesis, yet how
175 nucleolar RNA surveillance is set up to do so remains unresolved[10,12,14] . The 71 proteins
176 present in the SSU processome together with the 14 proteins present within the RNA
177 exosome provide a unique opportunity to screen pathway-wide protein-protein
178 interactions *in silico* using Alphafold-Multimer[22–24]. We employed this approach to obtain
179 an SSU processome predictome to test 3,570 unique binary interactions, which together
180 with our high-resolution cryo-EM maps enabled the identification of many previously
181 unknown interactions (**Fig. 2a, Extended Data Fig. 4, and Supplementary Table 3**).
182 These data highlight key features of the SSU biogenesis pathway including the
183 architectural roles of Sas10-domain containing complexes, tethering functions of Mpp10
184 for ribosomal protein S5 and Dim1, and predictions for the recruitment and activation of

185 Dhr1/DHX37 (**Extended Data Fig. 4d,f**). In addition, mutually exclusive interactions
186 between Kre33 and Faf1 or Bms1 are revealed, which now explain previously unassigned
187 density for the human homologs of Kre33/Faf1 (NAT10/C1ORF13) in the human SSU
188 processome[11] (**Extended Data Fig. 4e**).

189 A striking series of predicted interactions emerged from the SSU processome
190 predictome that suggest extensive contacts between the RNA degradation machinery and
191 the maturing and disassembling SSU processome **(Fig. 2a,b**). In addition to previously
192 known interactions between the RNA helicase Mtr4 and Utp18[ref14] and newly identified
193 multivalent interactions between the yeast Rrp6 C-terminus (lasso) and the SSU
194 processome in this study, the SSU processome predictome suggested that Utp14, the
195 essential activator of Dhr1, additionally serves as a bridge between Mtr4 (via Exosome
196 Recruitment Motif 1, ERM1), the core exosome component Rrp40 (via ERM2), and the
197 SSU processome (**Fig. 2a,b**). This mode of binding is similar to the binding of the RNA
198 exosome cofactor Mpp6[ref25], with Mpp6 motifs having a high degree of sequence similarity
199 to Utp14 ERM1 and ERM2 (**Extended Data Fig. 5a**).

200 Based on these predictions, a model emerges in which the RNA exosome contains
201 four contact points for the SSU processome, which in addition to Utp18 AIM and the C-
202 terminus of Rrp6 (lasso) include two peptides of Utp14 (ERM1 and ERM2) (**Fig. 2b**).
203 Synergistically, the 2.7 Ångstrom structure of State H highlights that elements of Rrp6,
204 Utp18 (AIM), and predicted Utp14 (ERM1 and ERM2) are all positioned in close proximity
205 to the 3′ end of the 5′ ETS where the Mtr4 helicase needs to unwind the 5′ETS for both
206 maturation and disassembly to occur (**Fig. 2c**). In State H, Utp14 occupies a strategic
207 position with key regulatory elements that respond to conformational changes of the entire

208 particle. Elements of Utp14 that will in later states provide a part of a Dhr1 binding site
209 (segment b) or activate Dhr1 (segments d and e) are sequestered in State H near
210 Sof1/Utp20 and Utp7/Utp1 respectively (**Fig. 2c,d).** Separately, the newly identified Utp14
211 hook (segment c) recruits the auto-inhibited Dhr1 and this inactive state is further
212 stabilized by N-terminal elements of Pno1 (**Supplementary Fig. 27i,l**). This arrangement
213 places ERM1 and ERM2 of Utp14 directly between segments b and c so that after
214 cleavage at site A1 all elements that bridge the SSU processome and the RNA exosome
215 are present near the 3′ end of the 5′ ETS (**Fig. 2c,d**).

216 The network consisting of Utp18, Rrp6 and Utp14 suggests that beyond exosome
217 catalytic function, connective redundancy may play a major role in ensuring correct
218 placement of the RNA exosome near the SSU processome. While prior data have
219 indicated that Utp18 AIM mutants are synthetically lethal in the absence of Rrp6[ref12,14],
220 the relative contributions of Rrp6 exonuclease activity and its ability to bind to the SSU
221 processome have remained unclear. Using yeast genetics we show that in the absence
222 of the Utp18 AIM, an inactive Rrp6 exonuclease (Y361A)[26] results in synthetic lethality,
223 suggesting that catalytic activity of Rrp6 becomes essential if Mtr4 helicase cannot be
224 correctly positioned (**Fig. 2e**). These data suggest that both positioning and the
225 redundancy in connections of the RNA exosome to the SSU processome is essential for
226 its function. Without the Utp18 AIM, three connections to the SSU processome remain
227 via the Rrp6 lasso and the predicted Utp14 ERM1 & ERM2 (**Fig. 2a-d**). Our genetic data
228 indicate that as long as any one of these connections is present, cell viability is
229 maintained. By contrast, synthetic lethality is observed if all four connections are disrupted
230 (**Fig. 2e**). Since the Rrp6 lasso is a multivalent binder of the SSU processome with four

binding sites, we could separately show that iterative Rrp6 C-terminal truncations in a genetic background lacking the Utp18 and Utp14 connections gradually reduce growth (**Extended Data Fig. 5**). The SSU processome predictome together with structural data and genetics reveal a highly redundant nucleolar tethering network that couples SSU processome maturation, disassembly and RNA quality control. These findings are further consistent with the visualization of the human homolog of Rrp6 (EXOSC10) in the immediate vicinity of nucleolar SSU precursors[27] .

Synchronized exosome-mediated disassembly

Elucidating the precise molecular mechanisms governing the controlled disassembly of the SSU processome remains a significant challenge, as current models lack the necessary sampling and resolution to mechanistically explain this process[9]. Here, States H-O capture a series of intermediates that follow RNA exosome-mediated disassembly (**Figs. 1 and 3**), allowing us to mechanistically explain how disassembly and RNA quality control are coupled. The irreversible 3′ to 5′ elimination of the 5′ ETS by the RNA exosome is directly coupled to the release of assembly factors in the exosome's path. These include, among others, the Sof1-Utp7 complex at the 5′ hinge, the UtpB complex at the 3′ hinge, and finally Utp18 and the UtpA complex positioned at the start of the 5′ ETS (**Fig. 3a**). RNA exosome-mediated compositional changes to the SSU processome result in three key events that occur concurrently. First, the reduction of multi-valent RNA-protein and protein-protein interactions within the SSU processome leads to release of bound and tethered complexes. Second, the RNA exosome loses two of its interaction sites with the SSU processome and its function transitions from substrate engagement to

254 substrate monitoring. Third, the changes of the SSU processome landscape provide new
255 binding surfaces for Utp14, which organizes both Dhr1 repositioning and activation (**Fig.**
256 **3**).

257 Beginning in State H, RNA exosome mediated processing of the 3′ end of the 5′
258 ETS alters the Sof1 binding site, weakening its interaction with Utp7 until only the C-
259 terminus of Utp7 remains bound in State I. During this transition, key regulatory elements
260 of Utp14 involved in subsequent Dhr1 recruitment (segment b) and activation (segments
261 d and e) are released while remaining tethered via peptides bound to Dhr1 and Pno1
262 (segments c and f respectively). During subsequent 5′ ETS degradation, represented in
263 states J and K, the Utp7 C-terminus is released, and its binding site is gradually occupied
264 by elements of Utp14 (segments a and b) that prepare a binding site for Dhr1 as the UtpC
265 complex is released. During the transition from State K to L, continued 5′ ETS processing
266 results in UtpB losing its primary binding site at the 3′ hinge while remaining tethered to
267 the SSU processome via Utp18, and Dhr1 remains connected to the particle via its N-
268 terminus and the Utp14 hook (segment c) (**Fig. 3b**). Following complete 5′ ETS removal
269 during the transition from State L to State M, UtpA, associated proteins, Utp18, and Rrp6
270 are fully released (**Fig. 3, Extended Data Fig. 6a**). During this key transition the roles of
271 the RNA exosome and Dhr1 are dramatically changed.

272 The role of the RNA exosome shifts from the active substrate engaged state with
273 four binding sites on the SSU processome to an overall surveillance state through the
274 remaining two Utp14 ERM sites (**Extended Data Fig. 6a**). Furthermore, re-engagement
275 of the substrate by the RNA exosome is prevented by the lack of a Utp18 binding site and
276 the occlusion of the Rrp6 lasso binding site by the C-terminus of ribosomal protein S4

277 (**Fig. 3b, Extended Data Fig. 6b and c**). Separately, the role of Dhr1 changes from a
278 tethered auto-inhibited state to a repositioned, substrate engaged, and activated enzyme
279 poised to remove U3 snoRNA from the pre-40*S* particle.
280

281 **Molecular circuitry of Dhr1 activation**

282 High-resolution crystal structures of Dhr1/DHX37 have shown that this DEAH-box
283 helicase in isolation can exist in two states, an inactive state in which an auto-inhibitory
284 loop prevents substrate binding, and an active state, in which single-stranded RNA acts
285 as a substrate[11,19]. However, thus far no Utp14-mediated active state of Dhr1 has been
286 observed. The comparison between the inactive state of Dhr1 in State H and the Utp14-
287 mediated active state of Dhr1 in State O now rationalizes how irreversible RNA exosome-
288 mediated 5′ ETS degradation orchestrates a cascade of events that triggers Dhr1
289 activation in a state-specific manner during SSU processome disassembly (**Fig. 4**).

290 In State H, the UtpB tetramer provides binding sites for both Dhr1 and Pno1
291 (elements 1 and 4), which enable additional elements of Pno1 (elements 2 and 3) to
292 stabilize the auto-inhibited state of Dhr1. Element 3 of Pno1 stabilizes the auto-inhibitory
293 loop of Dhr1, while element 2 of Pno1 prevents binding of segment d of Utp14, thus
294 preventing a switch towards Dhr1 activation (**Fig. 4a**). Separately, segments of Utp14 that
295 subsequently provide a binding site (segment b) or activate Dhr1 (segments d and e) are
296 sequestered by Utp20/Sof1 and Utp7-Utp1 respectively (**Figs. 2c, 4a, c**).

297 In State O, the prior RNA exosome-mediated elimination of the UtpB complex, and
298 the release of Utp14 segments a-e have dramatically changed the local environment for
299 Dhr1. The new Dhr1 binding site (Utp14 segments a and b) is formed on top of its

300 substrate U3 snoRNA, which still base-pairs with 18*S* elements that will form the central
301 pseudoknot upon Dhr1-mediated U3 snoRNA release (**Fig. 4b**). The relative positions of
302 Utp14 elements c and f now enable Utp14 elements d and e to stabilize a conformation
303 of Dhr1 in which the RecA lobes are dramatically shifted to engage the substrate U3
304 snoRNA while displacing the auto-inhibitory loop (**Fig. 4b, d**). The architecture of the
305 Utp14-mediated active form of Dhr1 in State O rationalizes a wealth of genetic and
306 biochemical data from yeast and mammalian systems, highlighting that this mode of
307 activation is distinct from G-patch mediated DEAH-box helicase activation (**Extended**
308 **Data Fig. 6e-g**)[19,21].

309 Thus, RNA exosome-mediated remodeling of the SSU processome triggers a
310 series of compositional and conformational changes within the disassembling SSU
311 processome that collectively switch Dhr1 from an "OFF" into an "ON" state that enables
312 its engagement and processing of U3 snoRNA. The irreversible release of U3 snoRNA
313 and the formation of the central pseudoknot prepare the resulting pre-40*S* particle for
314 subsequent nuclear maturation where Utp14 is replaced by Nob1[ref2], releasing the final
315 link to nucleolar RNA surveillance.

316

317 **Conclusions**

318 Nuclear bodies that contain biosynthetic processing pathways such as the nucleolus,
319 Cajal bodies, and nuclear speckles share unified organizational principles by which RNA
320 synthesis and processing results in the formation and dynamics of these multi-valent
321 condensates[28,29]. For nucleolar SSU processome maturation and disassembly, we
322 present a high-resolution temporal perspective, highlighting that this highly dynamic

323 process is driven by the activities of two RNA helicases associated with the RNA
324 degradation machinery (Mtr4) and the SSU processome itself (Dhr1) (**Figs. 1 and 2**). The
325 irreversible unwinding and degradation of pre-ribosomal RNA (5′ ETS) changes the
326 composition of disassembling SSU processomes, allowing regulatory peptides of Utp14
327 to probe the changing landscape of these particles to state-specifically reposition and
328 activate Dhr1 for the terminal and irreversible release of U3 snoRNA (**Figs. 3 and 4**). The
329 emerging model now highlights the importance of multivalent tethering at three levels.
330 First, intra-SSU processome tethering enables pre-recruitment of assembly factors
331 required for subsequent steps including restructuring of the SSU processome and A1
332 cleavage. Second, the extent (valency) of tethering between large particles such as the
333 RNA exosome to the SSU processome changes as the exosome matures and
334 disassembles the SSU processome, thereby shifting the role of the RNA exosome from
335 initial recognition to substrate engagement and finally substrate surveillance. Third, at the
336 level of the organelle, overall tethering of the maturing and disassembling SSU
337 processomes to the nucleolus is decreased as more and more nucleolar assembly factors
338 are released, thereby reducing the overall valency of particles before nucleolar release
339 (**Fig. 5**). These data suggest that rather than the loss of non-specific interactions within a
340 biomolecular condensate, it is the loss of specific protein-protein and protein-RNA
341 interactions that enables the release of pre-ribosomal particles from the nucleolus. The
342 scope of our study now allows us to illustrate molecular events at the Ångstrom scale that
343 can rationalize the organizational principles at the micrometer scale as observed for the
344 nucleolus[27]. This study highlights molecular transitions in large dynamic RNA-protein

complexes driven by RNA helicases, and how these changes may be coupled to movement through biomolecular condensates in nuclear bodies.

REFERENCES

1. Dragon, F. *et al.* A large nucleolar U3 ribonucleoprotein required for 18S ribosomal RNA biogenesis. *Nature* **417**, 967–970 (2002).

2. Dörner, K., Ruggeri, C., Zemp, I. & Kutay, U. Ribosome biogenesis factors—from names to functions. *Embo J* e112699 (2023) doi:10.15252/embj.2022112699.

3. Broeck, A., Vanden & Klinge, S. Eukaryotic Ribosome Assembly. *Annual Review of Biochemistry* **Volume 93 (In press)**, (2024).

4. Kornprobst, M. *et al.* Architecture of the 90S Pre-ribosome: A Structural View on the Birth of the Eukaryotic Ribosome. *Cell* **166**, 380–393 (2016).

5. Chaker-Margot, M., Barandun, J., Hunziker, M. & Klinge, S. Architecture of the yeast small subunit processome. *Science* **355**, eaal1880 (2017).

6. Sun, Q. *et al.* Molecular architecture of the 90S small subunit pre-ribosome. *Elife* **6**, e22086 (2017).

7. Barandun, J. *et al.* The complete structure of the small-subunit processome. *Nat. Struct. Mol. Biol.* **24**, 944–953 (2017).

8. Cheng, J., Kellner, N., Berninghausen, O., Hurt, E. & Beckmann, R. 3.2-Å-resolution structure of the 90S preribosome before A1 pre-rRNA cleavage. *Nat. Struct. Mol. Biol.* **24**, 954–964 (2017).

9. Cheng, J. *et al.* 90S pre-ribosome transformation into the primordial 40S subunit. *Science* **369**, 1470–1476 (2020).

10. Du, Y. *et al.* Cryo-EM structure of 90S small ribosomal subunit precursors in transition states. *Science* **369**, 1477–1481 (2020).

11. Singh, S., Broeck, A. V., Miller, L., Chaker-Margot, M. & Klinge, S. Nucleolar maturation of the human small subunit processome. *Science* **373**, eabj5338 (2021).

12. Lau, B. *et al.* Structure of the Maturing 90S Pre-ribosome in Association with the RNA Exosome. *Mol. Cell* **81**, 293-303.e4 (2021).

13. Broeck, A. V. & Klinge, S. An emerging mechanism for the maturation of the Small Subunit Processome. *Current Opinion in Structural Biology* **73**, 102331 (2022).

14. Thoms, M. *et al.* The Exosome Is Recruited to RNA Substrates through Specific Adaptor Proteins. *Cell* **162**, 1029–1038 (2015).

15. Hunziker, M. *et al.* Conformational switches control early maturation of the eukaryotic small ribosomal subunit. *Elife* **8**, 213 (2019).

16. Keidel, A., Long, C. L., Iwasa, J. & Conti, E. RNA-Degrading Exosome Complexes: Molecular Mechanisms and Structural Insights. *Annu. Rev. Cell Dev. Biol.* (2025) doi:10.1146/annurev-cellbio-111822-115115.

17. Sardana, R. *et al.* The DEAH-box helicase Dhr1 dissociates U3 from the pre-rRNA to promote formation of the central pseudoknot. *PLoS Biol* **13**, e1002083 (2015).

18. Zhu, J., Liu, X., Anjos, M., Correll, C. C. & Johnson, A. W. Utp14 recruits and activates the RNA helicase Dhr1 to undock U3 snoRNA from the pre-ribosome. *Molecular and Cellular Biology* **36**, MCB.00773-15 (2016).

19. Boneberg, F. M. *et al.* Molecular mechanism of the RNA helicase DHX37 and its activation by UTP14A in ribosome biogenesis. *RNA* **25**, 685–701 (2019).

20. Choudhury, P., Hackert, P., Memet, I., Sloan, K. E. & Bohnsack, M. T. The human RNA helicase DHX37 is required for release of the U3 snoRNP from pre-ribosomal particles. *RNA Biol* **16**, 54–68 (2018).

21. Lin, R., Elmir, E., Reynolds, M. J. & Johnson, A. W. In vitro characterization of the yeast DEAH/RHA RNA helicase Dhr1. *J. Biol. Chem.* **301**, 108366 (2025).

22. Evans, R. *et al.* Protein complex prediction with AlphaFold-Multimer. *bioRxiv* 2021.10.04.463034 (2021) doi:10.1101/2021.10.04.463034.

23. Yu, D., Chojnowski, G., Rosenthal, M. & Kosinski, J. AlphaPulldown—a python package for protein–protein interaction screens using AlphaFold-Multimer. *Bioinformatics* **39**, btac749 (2022).

24. Schmid, E. W. & Walter, J. C. Predictomes, a classifier-curated database of AlphaFold-modeled protein-protein interactions. *Mol. Cell* **85**, 1216-1232.e5 (2025).

25. Wasmuth, E. V., Zinder, J. C., Zattas, D., Das, M. & Lima, C. D. Structure and reconstitution of yeast Mpp6-nuclear exosome complexes reveals that Mpp6 stimulates RNA decay and recruits the Mtr4 helicase. *eLife* **6**, e29062 (2017).

26. Assenholt, J. *et al.* Exonucleolysis is required for nuclear mRNA quality control in yeast THO mutants. *RNA (N. York, NY)* **14**, 2305–13 (2008).

407 27. Quinodoz, S. *et al.* Mapping and engineering RNA-controlled architecture of the
408 multiphase nucleolus. *bioRxiv* 2024.09.28.615444 (2024)
409 doi:10.1101/2024.09.28.615444.

410 28. Quinodoz, S. A. & Guttman, M. Essential Roles for RNA in Shaping Nuclear
411 Organization. *Cold Spring Harb. Perspect. Biol.* **14**, a039719 (2021).

412 29. Shan, L., Li, P., Yu, H. & Chen, L.-L. Emerging roles of nuclear bodies in genome
413 spatial organization. *Trends Cell Biol.* **34**, 595–605 (2024).

414

415 **METHODS**

416 **Generation of endogenously tagged DHR1, KRE33, UTP7 and UTP14 strains**

417 Assembly intermediates of the *S. cerevisiae* SSU processomes were purified from
418 three genetically modified BY4741 (MATa his3Δ leu2Δ0 met15Δ0 ura3Δ0) strains. Where
419 genes of interest (DHR1, KRE33, UTP7 and UTP14) were endogenously tagged: the first
420 strain containing C-terminal tandem 3C protease-cleavable mCherry and TEV-cleavable
421 alfa peptide tag on DHR1 along with a 3C cleavable C-terminal GFP-tag on KRE33 (MATa
422 his3Δ leu2Δ0 met15Δ0 ura3Δ0 DHR1-linker-tev-alfa tag-3c-mCherry under Hygromycin
423 B selection and KRE33-linker-tev-GFP under Nourseothricin selection), the second strain
424 containing only C-terminal tandem 3C protease-cleavable mCherry and TEV-cleavable
425 alfa peptide tag on DHR1 (MATa his3Δ leu2Δ0 met15Δ0 ura3Δ0 DHR1-linker-tev-alfa
426 tag-3c-mCherry under Hygromycin B selection) and the third strain containing C-terminal
427 tandem 3C protease-cleavable mCherry and a TEV-cleavable alfa peptide tag on DHR1
428 along with TEV cleavable C-terminal GFP-tag on UTP7 and C-terminally streptavidin-
429 binding-peptide (sbp) tag on UTP14 (MATa his3Δ leu2Δ0 met15Δ0 ura3Δ0 DHR1-linker-
430 tev-alfa tag-3c-mCherry under Hygromycin B selection and UTP7-linker-tev-GFP under
431 G418 selection and UTP14-linker-SBP under Nourseothricin selection). The three strains

432 were generated with standard genomic tagging techniques using the following primers for
433 yeast genomic tagging:
434 DHR1 forward primer:
435 TCACCAGAAAGGGCTTCCAGACCATCACAGGTGAAGAGAAAGAAAAAAAAACGCT
436 GCAGGTCGACGGATCC
437 DHR1 reverse primer:
438 TTAAGTGGTTGCAATTATTTGATGCCCTAGATAGGAATAATGTATTCTTCGGCAGAT
439 CCGCGGCCGCATAGG
440 Kre33 forward primer:
441 AAGAGATGAAAGCTATGAAAAAACCAAGAAAGTCTAAAAAGGCTGCAAATACGCTG
442 CAGGTCGACGGATCC
443 KRE33 reverse primer :
444 TGTAAAGGTTCAAACATCAACTATGTTTCTATTCTATATTATTGTACAAAGGCAGATC
445 CGCGGCCGCATAGG
446 UTP7 forward primer:
447 TTTCAGAAGACCACAAGGATGTCATCGAAGAGGCATTGAGCAGATTCGGCACGCT
448 GCAGGTCGACGGATCC
449 UTP7 reverse primer:
450 GCTATATTAATATGCAATCGATTCTCATACTGTCAACTTTTTGAACATGAGGCAGAT
451 CCGCGGCCGCATAGG
452 UTP14 forward primer:
453 TCATGACTAAGCCAGGCCAAGTTATTGATCCTTTGAAGGCACCATTTAAGACGCTG
454 CAGGTCGACGGATCC

455 UTP14 reverse primer:

456 ATTATTCCAGTATTACTATTCTACACAATGCATAATAAATAGATATAAAAGGCAGATC

457 CGCGGCCGCATAGG

458 The three strains were grown at 30 °C in YPD media (1% yeast extract, 2%

459 peptone and 2% glucose) to optical density of OD 1 measured at 600 nm. Cells were

460 harvested at 4,000*g* for 5 min, washed once with 1 l of ice cold ddH_2O and once with a

461 volume of ddH_2O supplemented with protease inhibitors (E64, pepstatin and PMSF) equal

462 to the mass of the cell pellet. The final pellets of ~30-40g were flash frozen in liquid

463 nitrogen. Pellets were lysed by cryo-grinding using a Retsch Planetary Ball Mill PM100

464 and powder was stored at –80 °C.

465

466 **Purification of SSU processome intermediates**

467 Cryo-ground powder was resuspended with buffer 1 (60mM Tris pH7.5, 50mM

468 NaCl, 2mM MgCl2, 5% glycerol, 0.1% NP-40) with addition of PMSF, pepstatin and E64

469 protease inhibitors. The suspension was cleared by centrifugation at 4 °C and 40,000*g*

470 for 20 min and lysate was incubated with 800 µl of packed NHS–sepharose beads

471 (Cytiva) coupled to anti-mCherry nanobodies for the first capture for all purifications and

472 incubated for 3.5 h at 4 °C on a nutator. Beads were pelleted by centrifugation at 4 °C for

473 1 min at 127*g*. After five washes in buffer 1, complexes were eluted in buffer EB (60mM

474 Tris, 50mM NaCl, 5mM MgCl2, 2% glycerol, 0.01% NP-40) supplemented with 3C

475 protease for 1 h at 4 °C. Beads were pelleted by centrifugation at 4 °C for 1 min at 127*g*

476 and supernatant was eluted and incubated with 80 µl of packed NHS–sepharose beads

477 (Cytiva) coupled to anti-GFP nanobodies for second capture (Dhr1/Kre33 and Dhr1/Utp14

478 purifications) while anti-alfa nanobodies were used for a second Dhr1 (Dhr1 only). Beads
479 were incubated for 1 h at 4 °C on a nutator and pelleted by centrifugation at 4 °C for 1 min
480 at 127*g* and washed twice with 2 ml of Buffer EB. After the second wash, for Dhr1/Kre33
481 and Dhr1 only purifications, beads were pelleted and resuspended with 25 µl of Buffer EB
482 supplemented with 1mM DTT and TEV protease and incubated on ice for 1 h. Beads
483 were pelleted by centrifugation at 4 °C for 10 min at 21,130g and the supernatant was
484 collected. For Dhr1/Utp14 purification, after the second capture (here Utp7), beads were
485 pelleted by centrifugation at 4 °C for 1 min at 127*g* and flowthrough was collected, the rest
486 of the beads were discarded (this step was used to remove earlier contaminating
487 complexes). The flowthrough was incubated with 40 µl of packed NHS–sepharose beads
488 (Cytiva) coupled to streptavidin for 1 h at 4 °C on a nutator. Beads were pelleted by
489 centrifugation at 4 °C for 1 min at 127*g* and washed twice with 2 ml of Buffer EB. After the
490 second wash, beads were pelleted and resuspended with 40 µl of Buffer EB
491 supplemented with 1mM DTT and 5 mM of D-biotin (Amresco) and incubated on ice for
492 20 min. Beads were pelleted by centrifugation at 4 °C for 10 min at 21,130g and the
493 supernatant was collected.
494
495 **Cryo-EM grid preparation and data acquisition**
496 Cryo-EM grids were prepared using a Vitrobot Mark IV robot (FEI Company) set
497 to 90% humidity and 18 °C temperature. Three and a half microliters of the eluted solution
498 was applied to a glow-discharged Quantifoil Au R3.5/1 with a layer of 2-nm ultrathin
499 carbon (LFH7100AR35, Electron Microscopy Sciences). After 2.5 min incubation inside
500 the Vitrobot chamber, the excess solution was manually blotted and a fresh sample of 3.5

501 µl was reapplied inside the Vitrobot chamber and incubated for another 2.5 min. The lower
502 the concentration of particles of a given preparation, the higher the number of applications
503 that were done on each grid. For the Dhr1 and Kre33 dataset, a total of five applications
504 were done on each grid. The grid was then blotted (blot force of 8 and blot time of 9 s)
505 and plunged into liquid ethane. For the Dhr1dataset, a total of two applications were done
506 for each grid. The grid was then blotted (blot force of 8 and blot time of 7 s) and plunged
507 into liquid ethane and for the Dhr1 and Utp14 dataset, a total of five applications were
508 done on each grid to achieve a good distribution of particles. The grid was then blotted
509 (blot force of 8 and blot time of 9 s) and plunged into liquid ethane. Grids were imaged on
510 a Titan Krios electron microscope (FEI) with an energy filter (slit width of 20 eV) and a K3
511 Summit detector (Gatan) operating at 300 kV with a nominal magnification of ×64,000.
512 SerialEM[30] was used to collect four datasets. 44,272 micrographs were collected
513 for the Kre33/Dhr1 dataset, two datasets of Dhr1 were collected totaling to 84,463
514 micrographs and 85,031 micrographs were collected for Dhr1 and Utp14 dataset. All
515 datasets were collected with a defocus range of −1 to −2.5 µm and a super-resolution
516 pixel size of 0.54 Å. Micrographs contained 40 frames using a total dose of 25.3-
517 30.8 e−per pixel per second (specimen pixel size of 1.08 Å per pixel) with an exposure
518 time of 2-2.5 s and a total dose of 61.7 -63.1e− Å−2. A multi-shot strategy was used to
519 record nine micrographs per hole at each stage position with the same defocus range,
520 electron dose and frame count.
521
522 **Cryo-EM data processing Dhr1 and Kre33 dataset**

523 The Dhr1 and Kre33 dataset was processed using a combination of RELION
524 5beta[31] and cryoSparc v4.6[ref32]. 44,272 movies were gain corrected, dose weighted,
525 aligned, with each dataset having different optic groups and binned to a pixel size of 1.08
526 Å using RELION's implementation of a MotionCor2-like algorithm[33]. Micrograph defocus
527 was estimated using Gctf[34] . Particles were picked using Laplacian (autopick) in RELION
528 5beta and post 2D classification a total of 2,817,609 particles were re-extracted at a pixel
529 size of 4.32 Å per pixel (4× binning) and underwent 3D classification in RELION 5beta
530 with alignment using a reference map from previous datasets. Two good classes were
531 combined, and duplicates were removed to result in 308,351 total particles. These
532 particles were subjected to three rounds of CTF refinement and Bayesian polishing in
533 RELION 5beta. Post polishing all homogenous refinements were completed in CryoSparc
534 v4.6 and classifications were all done in RELION 5beta, particle positions from cryosparc
535 are converted into RELION using pyem software csparc2star.py[35] . The polished particles
536 were subjected to a homogenous refinements resulting in a reconstruction at a global
537 resolution of 3.3 Å. To separate the states present in the consensus reconstruction,
538 multiple 3D classifications without alignment were performed. This was followed by 3D
539 variability[36] in CryoSparc v4.6 for analysis of the type of heterogeneity present in the data
540 which guided the creation of a mask around the region of interest and further 3D
541 classification without alignment on the region of variability. Eight distinct states (sates A-
542 G) were isolated from the dataset that showed unique features in the progression of
543 maturation of the SSU processome pathway (**Supplementary Fig.1**). The global
544 resolution of the eight states ranged from 3-5.9 Å.
545

546 **Cryo-EM data processing Dhr1 dataset**

547 Dhr1 dataset was processed using a combination of RELION 5beta[31] and
548 cryoSparc v4.6[ref32] . 84,463 movies were gain corrected, dose weighted, aligned, with
549 each dataset having different optic groups and binned to a pixel size of 1.08 Å using
550 RELION's implementation of a MotionCor2-like algorithm[33] . Micrograph defocus was
551 estimated using Gctf[34] . Particles were picked using crYOLO 1.7.5[37] and post 2D
552 classification a total of 13,198,550 particles were re-extracted at a pixel size of 4.32 Å per
553 pixel (4× binning) and underwent heterogenous refinement in CryoSparc v4.6 using a
554 reference map from previous classification in RELION 5beta. One good class was
555 isolated resulting in 1,933,969 total particles. These particles were subjected to three
556 rounds of CTF refinement and Bayesian polishing in RELION 5beta. Post polishing all
557 homogenous refinements were completed in CryoSparc v4.6 and classifications were all
558 done in RELION 5beta. Particle positions from cryosparc are converted into RELION
559 using pyem software csparc2star.py[35] . The polished particles were subjected to a
560 homogenous refinement resulting in a reconstruction at a global resolution of 3 Å. To
561 separate the states present in the consensus reconstruction, multiple iterations of 3D
562 classifications without alignment was performed. Followed by 3D variability[36] in
563 CryoSparc v4.6 for analysis of the type of heterogeneity present in the data which guided
564 the creation of a mask around the region of interest and further 3D classification without
565 alignment on the region of variability. Seven distinct states (sates H-N) were isolated from
566 the dataset that showed unique features in the progression of the disassembly of the SSU
567 processome pathway (**Supplementary Fig.2**). The global resolution of the seven states
568 ranged from 2.65-4.3 Å.

569

570 **Cryo-EM data processing Dhr1 and Utp14 dataset**

571 The Dhr1 and Utp14 dataset was processed using a combination of RELION
572 5beta[31] and cryoSparc v4.6[ref32] . 85,031 movies were gain corrected, dose weighted,
573 aligned, with each dataset having different optic groups and binned to a pixel size of 1.08
574 Å using CryoSparc v 4.6 motion correction. Micrograph defocus was estimated using
575 Patch CTF and particles were picked using a template picker resulting in a total of
576 27,069,273 particles which underwent heterogenous refinement and subsequent global
577 and local CTF refinements, followed by reference motion correction. Post polishing all
578 homogenous refinements were completed in CryoSparc v4.6 and classifications were all
579 done in RELION 5beta. Particle positions from cryosparc are converted into RELION
580 using pyem software csparc2star.py[35] . The polished particles were subjected to a
581 homogenous refinement resulting in a reconstruction at a global resolution of 2.9 Å. To
582 separate the states present in the consensus reconstruction, multiple iterations of 3D
583 classifications without alignment were performed. Followed by 3D variability[36] in
584 CryoSparc v4.6 for analysis of the type of heterogeneity present in the data which guided
585 the creation of a mask around the region of interest and further 3D classification without
586 alignment on the region of variability. State O was isolated from the dataset with global
587 resolution of 3.25 Å that showed clear density for Utp14-bound Dhr1 (**Supplementary**
588 **Fig. 3**).

589

590 **Generation of focused and composite maps for model buildings**

591 Composite maps for the total of 16 states were generated from combined focused
592 maps to facilitate model building. Focused maps were generated using subtraction and
593 refinement masks generated in CryoSparc v4.6. Each focused map was made by particle
594 subtraction with a masked region followed by masked local refinement. Local resolution
595 estimation for overall and all focused maps and filtering of the overall map were performed
596 using CryoSparc v4.6. Focused maps were combined into a composite map using the
597 'vop max' command in ChimeraX[38] (**Supplementary Figs. 4-25**).
598

599 **Model building and refinement**

600 A combination of AlphaFold structure predictions[39] , existing X-ray/EM structures,
601 and *de novo* model building was used to build the 16 SSU processome assembly
602 intermediates. A starting model (PDB: 5WLC/6KE6) that included all ribosomal proteins
603 and RNA was used as initial template for rigid body docking into the State H composite
604 map since it is of highest resolution. All template ribosomal protein models were manually
605 adjusted using COOT[40] . State H was then used as a template to build the proteins and
606 RNA into the other 15 states with manual adjustments in COOT. The final models for the
607 16 states were real-space refined with three cycles of refinement in PHENIX using
608 phenix.real_space_refine[41] using secondary structure restraints for proteins and RNA. In
609 regions with medium to low resolution, protein sidechains were trimmed to the C_β position
610 after all-atom refinement. The final model refinement statistics can be found in
611 **Supplementary Table 1**. The maps and models were analyzed and visualized in
612 ChimeraX[38] .
613

614 **SSU processome predictome**

615 Proteins present within States A-O together with 14 exosome proteins were
616 screened for binary interactions. The resulting 3570 unique interactions were screened
617 using the default settings in the AlphaPulldown[23] implementation of Alphafold-Multimer[22].
618 For the SSU processome predictome (**Fig. 2a**) the median iptm_ptm score of five models
619 was plotted (**Supplementary Table 3**).

620

621 **Yeast Growth Assays**

622 The *rrp6Δ utp14 Δ* strain and *rrp6Δ utp18 Δ utp14 Δ* strain in the BY4741
623 background were used for all studies. These strains were transformed with two yeast
624 centromeric vectors, one vector under URA3 selection bearing wild-type RRP6 and
625 UTP14 derived from pRSII416 and second vector under LEU2 selection bearing wild-type
626 RRP6 or rrp6 alleles containing mutations or c-terminal truncations in conjunction with
627 UTP14 wild-type or utp14 alleles containing mutations derived from pRSII415. Strains
628 carrying both pRSII415 and pRSII416 plasmids were selected on minimal media (SD-Ura
629 and Leu) after transformation. Colonies grown on the selection plates were selected and
630 grown in minimal media (SD-Ura and Leu) liquid cultures. Loss of the *URA3* plasmid was
631 done on minimal media agar plates (SD–Leu + 5-FOA) plates by spotting serial 10-fold
632 dilutions (starting at OD_{600} of 1) of liquid cultures. Growth was monitored at 30°C over a
633 period of 5 days.

634

635 **Data availability**

636 Raw unaligned multi-frame movies and aligned micrographs have been deposited in the
637 Electron Microscopy Public Image Archive (EMPIAR). The cryo-EM maps and atomic
638 models have been deposited in the Electron Microscopy Data Bank (EMDB) and the
639 Protein Data Bank (PDB): State A (EMD-49075, PDB 9N6V), State A* (EMD-49076, PDB
640 9N6W), State B (EMD-49077, PDB 9N6X), State C (EMD-49078, PDB 9N6Y), Sate D
641 (EMD-49079, PDB 9N6Z), Sate E (EMD-49080, PDB 9N70), State F (EMD-49082, PDB
642 9N72), State G (EMD-49083, PDB 9N73), State H (EMD-49084, PDB 9N74), State I
643 (EMD-49085, PDB 9N75), State J (EMD-49086, PDB 9N76), State K (EMD-49087, PDB
644 9N77), State L (EMD-49088, PDB 9N78), State M (EMD-49089, PDB 9N79), State N
645 (EMD-49090, PDB 9N7A), State O (EMD-49091, PDB 9N7B).
646

647 **ADDITIONAL REFERENCES:**

648 30. Mastronarde, D. N. Automated electron microscope tomography using robust
649 prediction of specimen movements. *J Struct Biol* **152**, 36–51 (2005).

650 31. Kimanius, D., Dong, L., Sharov, G., Nakane, T. & Scheres, S. H. W. New tools for
651 automated cryo-EM single-particle analysis in RELION-4.0. *Biochem J* **478**, 4169–4185
652 (2021).

653 32. Punjani, A., Rubinstein, J. L., Fleet, D. J. & Brubaker, M. A. cryoSPARC: algorithms
654 for rapid unsupervised cryo-EM structure determination. *Nat Methods* **14**, 290–296
655 (2017).

656 33. Zheng, S. Q. *et al.* MotionCor2: anisotropic correction of beam-induced motion for
657 improved cryo-electron microscopy. *Nat Methods* **14**, 331–332 (2017).

658 34. Zhang, K. Gctf: Real-time CTF determination and correction. *J Struct Biol* **193**, 1–12
659 (2016).

660 35. Asarnow, D., Cheng, D. A. E. P. Y. & Cheng, Y. UCSF pyem v0.5. Zenodo. (2019)
661 doi:10.5281/zenodo.3576630.

36. Punjani, A. & Fleet, D. J. 3D variability analysis: Resolving continuous flexibility and discrete heterogeneity from single particle cryo-EM. *J. Struct. Biol.* **213**, 107702 (2021).

37. Wagner, T. *et al.* SPHIRE-crYOLO is a fast and accurate fully automated particle picker for cryo-EM. *Commun Biol* **2**, 218–13 (2019).

38. Pettersen, E. F. *et al.* UCSF ChimeraX : Structure visualization for researchers, educators, and developers. *Protein Sci* **30**, 70–82 (2020).

39. Jumper, J. *et al.* Highly accurate protein structure prediction with AlphaFold. *Nature* **596**, 583–589 (2021).

40. Casañal, A., Lohkamp, B. & Emsley, P. Current Developments in Coot for Macromolecular Model Building of Electron Cryo-microscopy and Crystallographic Data. *Protein Sci.* pro.3791 (2019) doi:10.1002/pro.3791.

41. Afonine, P. V. *et al.* Real-space refinement in PHENIX for cryo-EM and crystallography. *Acta Crystallogr D Struct Biol* **74**, 531–544 (2018).

42. Black, J. J., Sardana, R., Elmir, E. W. & Johnson, A. W. Bud23 promotes the final disassembly of the small subunit Processome in Saccharomyces cerevisiae. *PLoS Genet.* **16**, e1009215 (2020).

Acknowledgements

We would like to thank M. Ebrahim, J. Sotiris, and H. Ng at the Evelyn Gruss Lipper Cryo-Electron Microscopy Resource Center at The Rockefeller University for assistance with grid screening and data collection. Mass spectrometry data was generated by the Proteomics Resource Center at The Rockefeller University (RRID:SCR_017797) using instrumentation funded by the Sohn Conferences Foundation and the Loena M. and Harry B. Helmsley Charitable Trust, and we particularly thank H. Molina, S. Heissel, and C. Peralta for assistance. We thank A. Vanden Broeck for advice with cryo-EM data processing and scripts for figures. We also thank K. Ye for sharing experimental data from a prior study[10] and members of the Klinge laboratory for critical reading of this manuscript.

Author Contributions

S.K. conceived the study. O.B. and S.K. designed the experiments and analyzed data. O.B. performed all experiments, including strain generation, complex purification, cryo-EM data processing, model building, and yeast genetics studies. All authors wrote and edited the manuscript.

Author information

Laboratory of Protein and Nucleic Acid Chemistry, The Rockefeller University, New York, NY, USA

Sebastian Klinge, Olga Buzovetsky

Corresponding author

Correspondence to Sebastian Klinge (klinge@rockefeller.edu).

Ethics declarations

The authors declare no competing interests.

Funding

Research reported in this publication was supported by the National Institute of General Medical Sciences of the National Institutes of Health under Award Numbers R01GM145950 and R35GM156426, and the Chan Zuckerberg Initiative Exploratory Cell Network.

712

713 **FIGURE LEGENDS**

714 **Fig. 1. SSU processome maturation and disassembly pathway.**

715 Simplified atomic models of the SSU processome assembly pathway with color-coded
716 rRNAs and ribosome assembly factors. Major changes in the rRNA between states are
717 in the foreground and changes in protein compositions as well as functions are noted.
718 Movements are indicated by arrows and protein or RNA elements that become ordered
719 or depart between different assembly intermediates are highlighted with black outlines.
720 The overall resolution of each cryo-EM reconstruction is noted below each state. A
721 dashed arrow indicates tethering of protein components. Major structural features such
722 as the left and right foot (LF and RF) along with the platform (Plat) are annotated in State
723 O.

724 **Fig. 2. Interaction networks between SSU processome and the RNA exosome.**

725 (**a**) Yeast SSU processome predictome containing assembly factors (AFs), ribosomal
726 proteins (RPs) and RNA exosome proteins (EXO) with color-coded confidence scores.
727 Three AlphaFold-Multimer predictions are highlighted with color-coded proteins and
728 confidence levels (pLDDT). (**b**) AlphaFold predictions for color-coded Utp14, Mtr4, and
729 Utp18 AIM mapped onto a composite model of the RNA exosome with Rrp6 (PDBs 5vzj
730 and 6d6q). (**c**) Cartoon representation of state H (left) and zoomed-in view (right) of the
731 5′ ETS 3′ end exit site (orange circles) with color-coded exosome interacting proteins.
732 Regulatory elements of Utp14 are highlighted in orange. (**d**) Schematic of Utp14, Rrp6,
733 Utp18, and Pno1 protein sequences in State H with interacting and functional elements

734 labeled. (**e**) Growth analysis of Rrp6 and Utp14 mutants in a Utp18 multi-Ala background
735 on 5-FOA plates.

736 **Fig. 3. Helicase-mediated disassembly is coupled to RNA quality control.**

737 (**a**) Schematic of SSU processome disassembly as a function RNA degradation. RNA and
738 protein elements bound to the 5′ ETS RNA are displayed as colored boxes and states
739 with corresponding 5′ ETS length are listed below. (**b**) Architecture of the changes around
740 the 5′ ETS exit sites (orange circles) from State H to M. Protein elements are color-coded
741 and elements of Utp14 (b-f), Pno1 (1-4) and the state of Dhr1 are highlighted.

742 **Fig. 4. Mechanism of Utp14-mediated Dhr1 activation.**

743 (**a**) Zoomed-in view of inactive Dhr1 in State H, with auto-inhibitory loop (light pink) and
744 inhibitory elements of Pno1 (1-4) and elements of Utp14 highlighted. The arrow indicates
745 the conformational change of Dhr1 RecA domains. (**b**) Zoomed-in view of activated Dhr1
746 in State O. Activating Utp14 elements (a, b, d, and e) are highlighted in orange. (**c**)
747 Schematic of State H molecular circuitry between Utp14, Dhr1 and Pno1. Interacting
748 elements are colored grey and inhibitory interactions are indicated with red lines. (**d**)
749 Schematic of State O molecular circuitry between Utp14, Dhr1 and Pno1. Interacting
750 elements are colored grey and activating interactions are indicated with green lines.

751 **Fig. 5. Model of the mechanism of SSU biogenesis in the nucleolus.**

752 (**a**) Schematic model of yeast SSU biogenesis in the nucleolus. Decreasing valency of
753 maturing particles is indicated below. (**b**) SSU processome maturation and disassembly
754 pathway with key transitions are indicated. Color-coded tethered proteins and complexes
755 are indicated with linkers. Arrows and numbers highlight the order of transition steps (RNA

756 degradation, conformational changes, protein release, or protein repositioning to new
757 binding sites) that lead to particles with low valency during disassembly.
758
759 **EXTENDED DATA FIGURE LEGENDS**
760 **Extended Data Fig. 1. Cryo-EM maps and models of the SSU processomes.**
761 (**a**) Composite cryo-EM maps and (**b**) atomic models colored by protein components
762 highlighting stepwise maturation of the SSU processome.
763 **Extended Data Fig. 2. rRNA compaction and folding events across states.**
764 (**a**) Compaction of the 18*S* 5′ domain from States A-C side view (left) and top view (right).
765 Labeled RNA elements are color coded. Arrows highlight compaction between states A
766 and C. (**b**) Simplified rRNA folding events leading up to A1 cleavage. (**c**) Compaction of
767 the central and 5′ domains during states I-M.
768 **Extended Data Fig. 3. Molecular proofreading for A1 cleavage during SSU**
769 **processome maturation.** Detailed views involving states prior to (States C, D, E) and
770 after A1 cleavage (State G) with color-coded proteins. The A1 cleavage site, U3
771 architectural sites, and active site of Utp24 are highlighted and flexible interactions
772 indicated by dashed lines.
773 **Extended Data Fig. 4. Yeast SSU processome predictome.**
774 (**a**) Color coded yeast SSU processome predictome between assembly factors (AFs),
775 ribosomal proteins (RPs) and RNA exosome proteins (EXO). Key interactors of Mpp10,
776 Kre33, Utp14, Dhr1 and Bfr2 are color coded. (**b**) State C containing proteins listed in (a).
777 (**c**) State H containing proteins listed in (a). (**d**) Sas10-domain containing Rrp6/Rrp47
778 complex and predicted Bfr2-Lcp5, and Mpp10-Sas10 complexes. The schematic of

779 Mpp10 contextualizes predictions of Mpp10 interactors. (**e**) Mutually exclusive
780 interactions with Kre33 (human NAT10) predicted for Bms1 and Faf1 (human C1orf131).
781 (**f**) Predictions of Dhr1/DHX37 interactions. Mutually exclusive binding of Pno1 and Utp14
782 to yeast Dhr1 are highlighted. Elements of human UTP14 known to activate human
783 DHX37 (MIDL, MIEF)[19] are indicated. Confidence levels (pLDDT) are color coded for
784 each protein.

785 **Extended Data Fig. 5. Yeast growth assays.**

786 (**a**) Schematics of Utp18, Rrp6, Mpp6, and Utp14 with interacting and functional elements
787 labeled with multi-Ala mutations used in this study as well as an alignment to Mpp6
788 exosome recruitment motif, indicated in grey. Designed truncations of Rrp6 lasso (bottom
789 left) with interacting and functional elements labeled. Locations of all alanine substitutions
790 for Utp18, Rrp6, and Utp14 are indicated on the right. (**b**) Growth analysis of Utp18 multi-
791 Ala mutant in Δrrp6 and Δutp14 background (top and middle panels) and Utp18 WT in
792 Δrrp6 and Δutp14 background (bottom panel). Growth assay using WT, truncations and
793 mutant Rrp6 or Utp14 constructs in the absence of genomic Rrp6 and Utp14. Colonies
794 sequenced are indicated on the right of the growth assays.

795 **Extended Data Fig. 6. Functional elements of Utp14, Rrp6, Utp18 and Dhr1.**

796 (**a**) Schematics of Utp14, Utp18 and Rrp6 across States A-O. Utp14 functional sequence
797 elements structured, bound, relocated, or activating are indicated on the left and the
798 presence/absence of Utp18 is indicated in the middle. Visible regions of the Rrp6 C-
799 terminus (lasso) are indicated on the right. (**b**) Binding of Rrp6 lasso to ribosomal proteins
800 S24 in State L. (**c**) Rrp6 exclusion by ES6D and S4 in State M. (**d**) State C highlights the
801 initial binding of the Rrp6 lasso and the initial sequestration of Utp14 elements a and b

802 that later recruit Dhr1. (**e**) Previously characterized mutations[18,42] mapped onto Dhr1 and
803 Utp14 represented in State O. Functional elements of Utp14 are shown in orange. (**f**)
804 Mode of Dhr1 activation by Utp14 in State O. (**g**) Mode of activation of DHX15 by G-patch
805 protein NKRF (PDB: 6SH7).
806
807

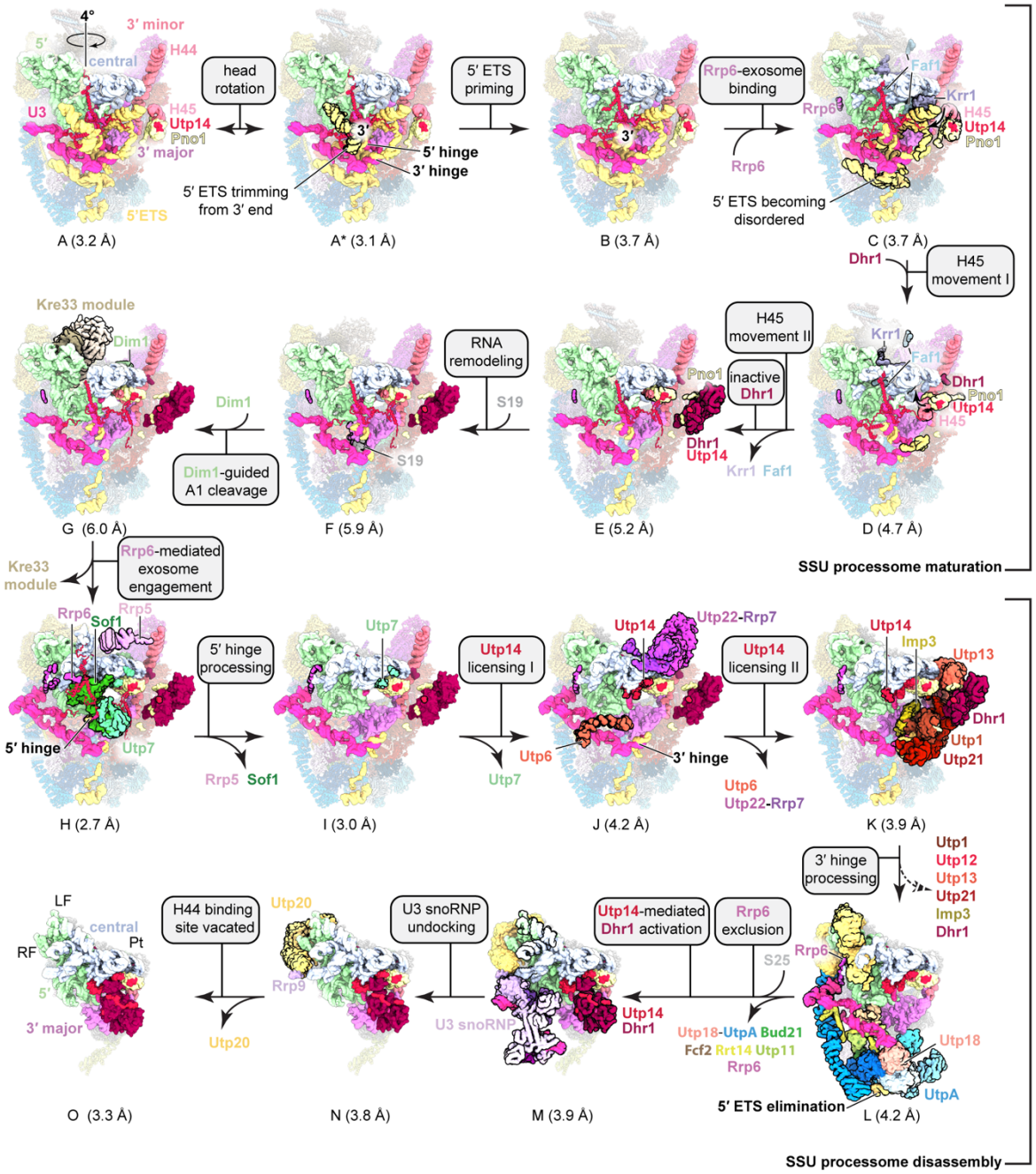

Fig. 1. SSU processome maturation and disassembly pathway.

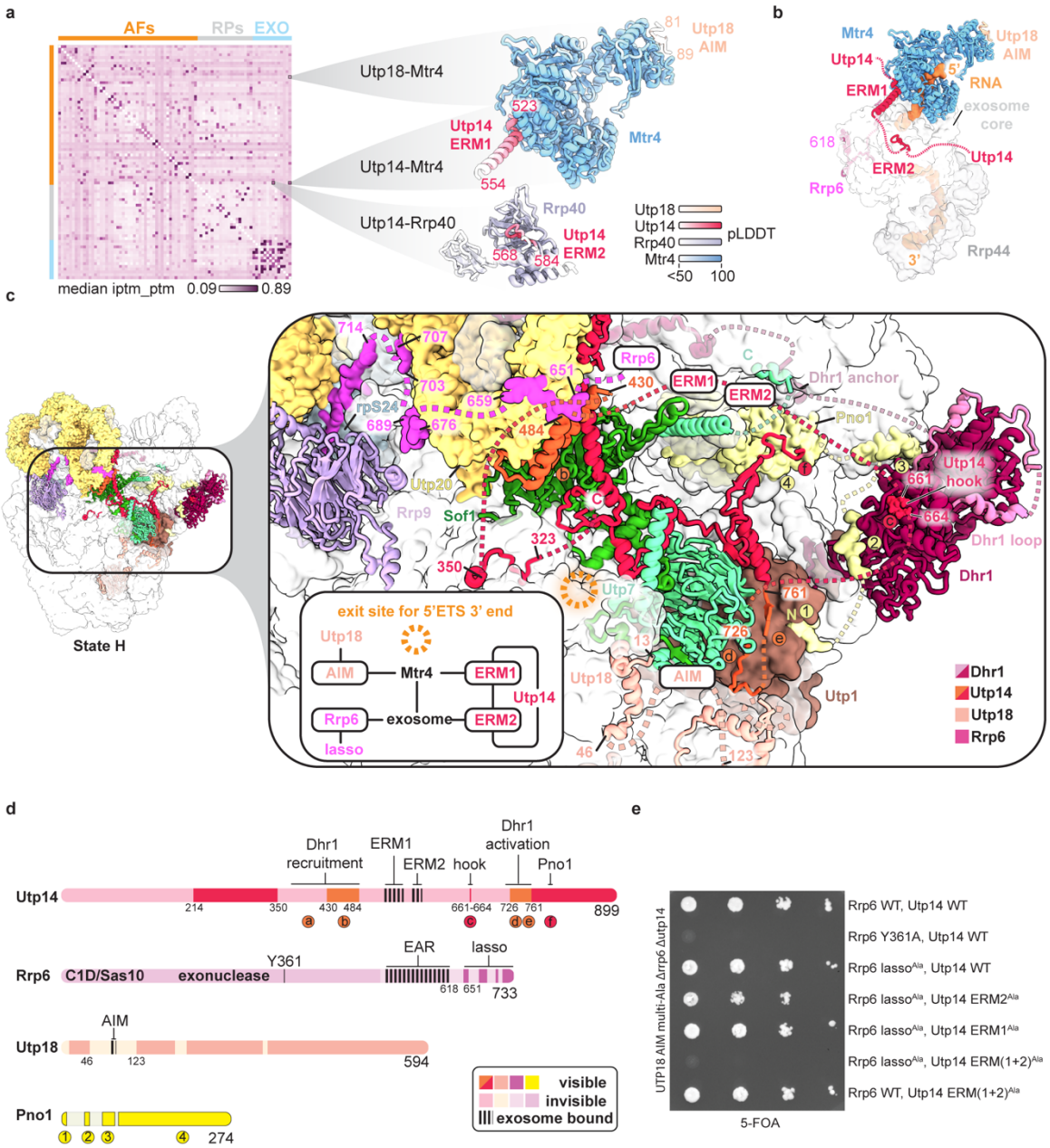

Fig. 2. Interaction networks between SSU processome and the RNA exosome.

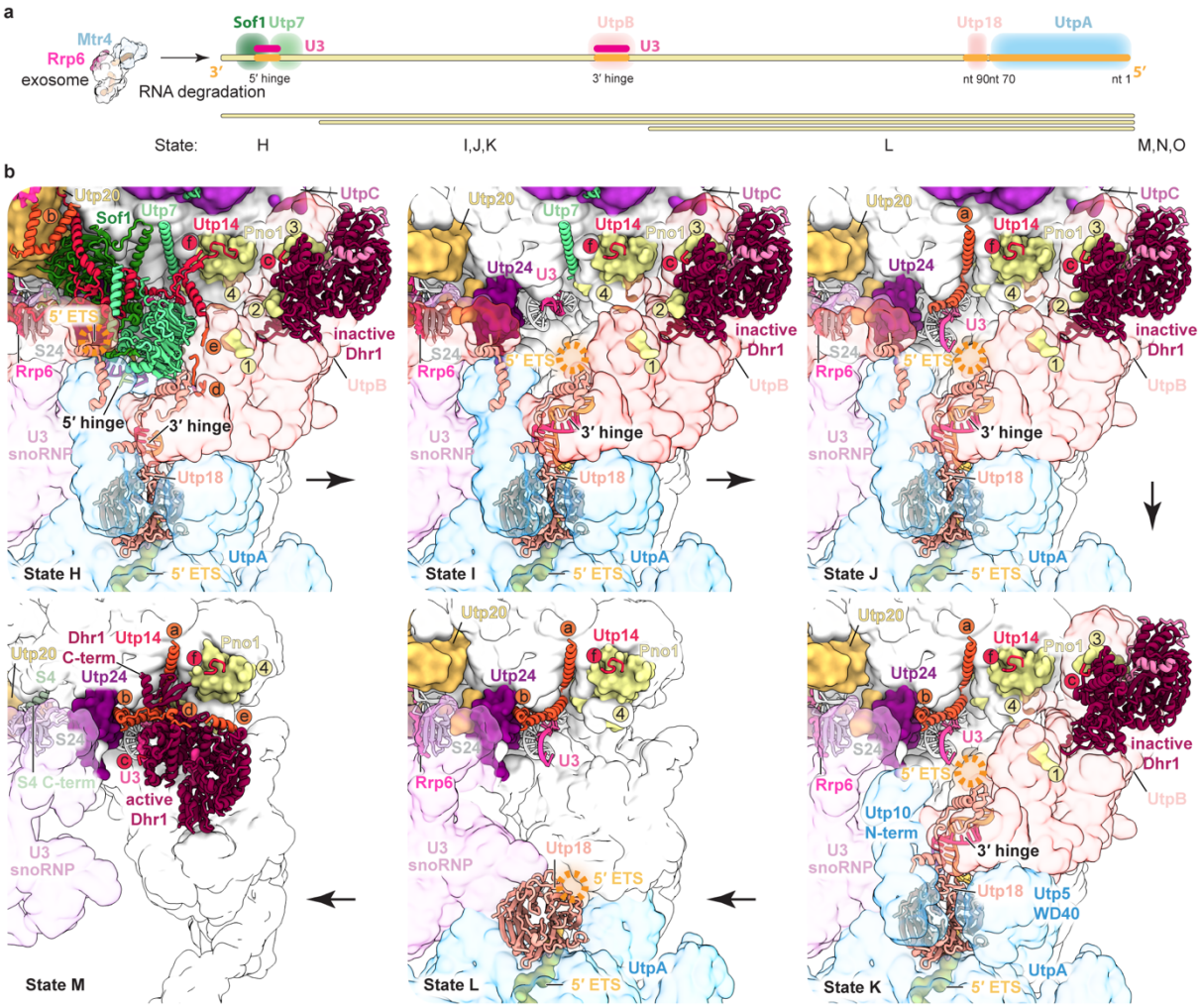

Fig. 3. Helicase-mediated disassembly is coupled to RNA quality control.

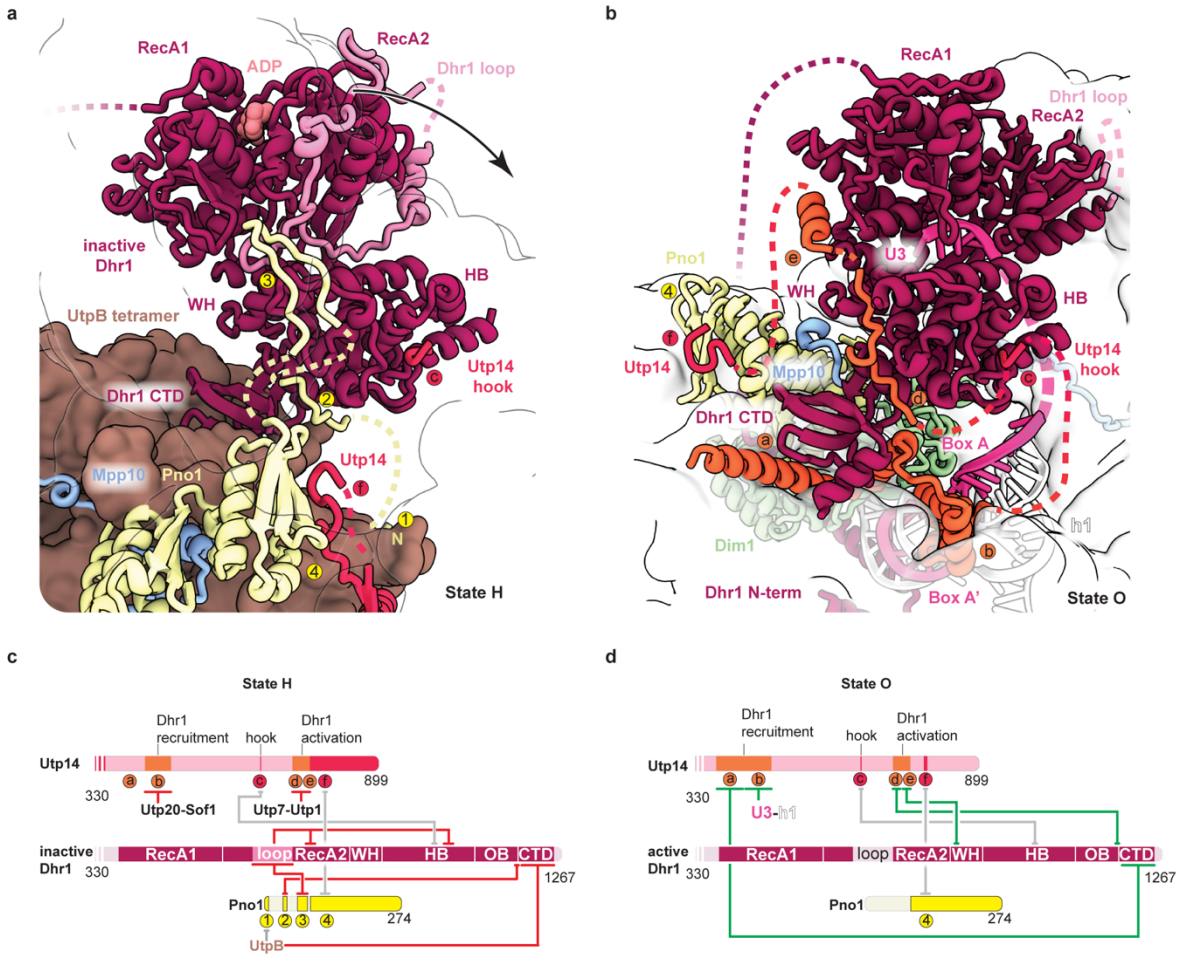

Fig. 4. Mechanism of Utp14-mediated Dhr1 activation.

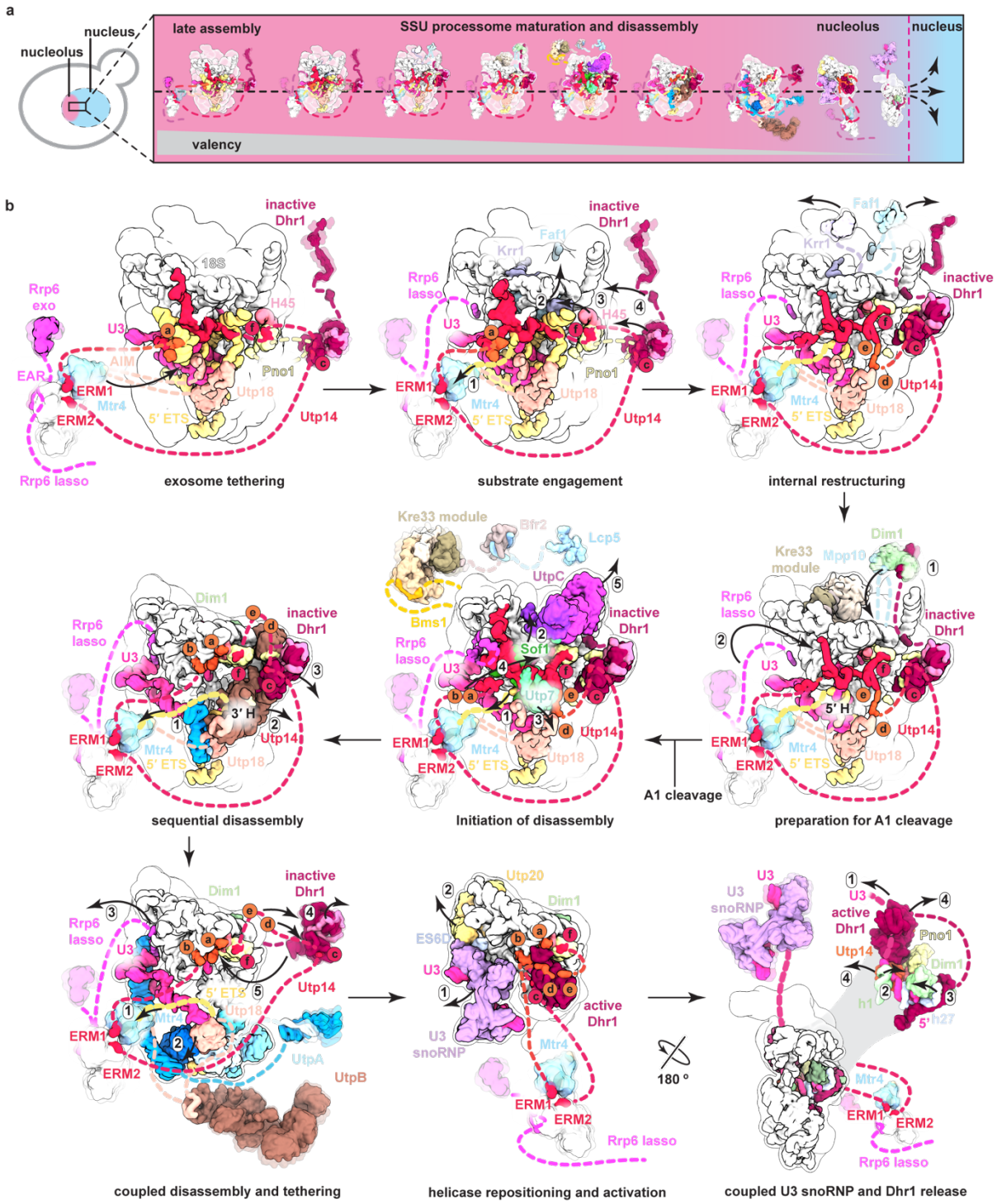

Fig. 5. Model of the mechanism of SSU biogenesis in the nucleolus.

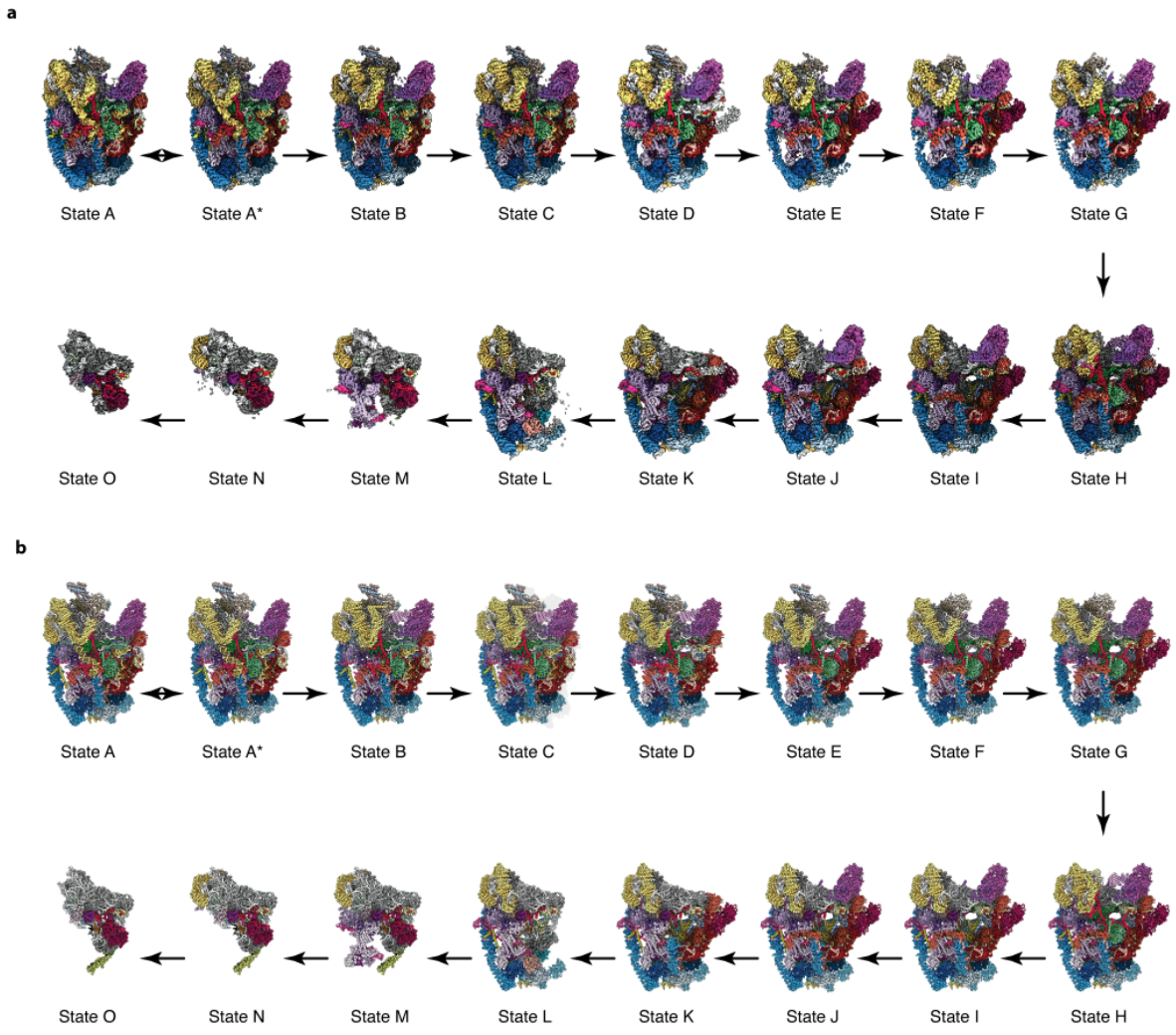

Extended Data Fig. 1. Cryo-EM maps and models of the SSU processomes.

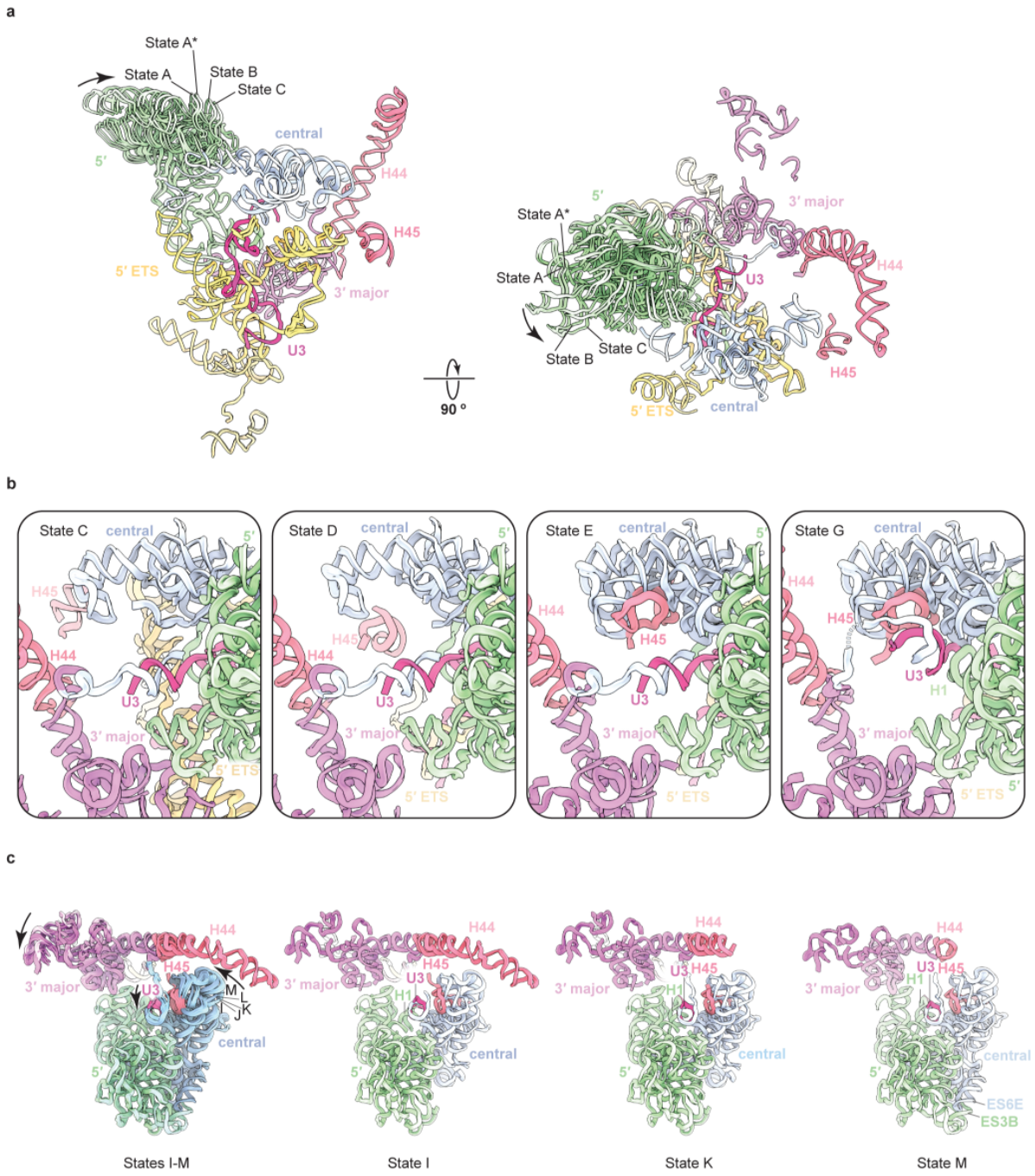

Extended Data Fig. 2. rRNA compaction and folding events across states.

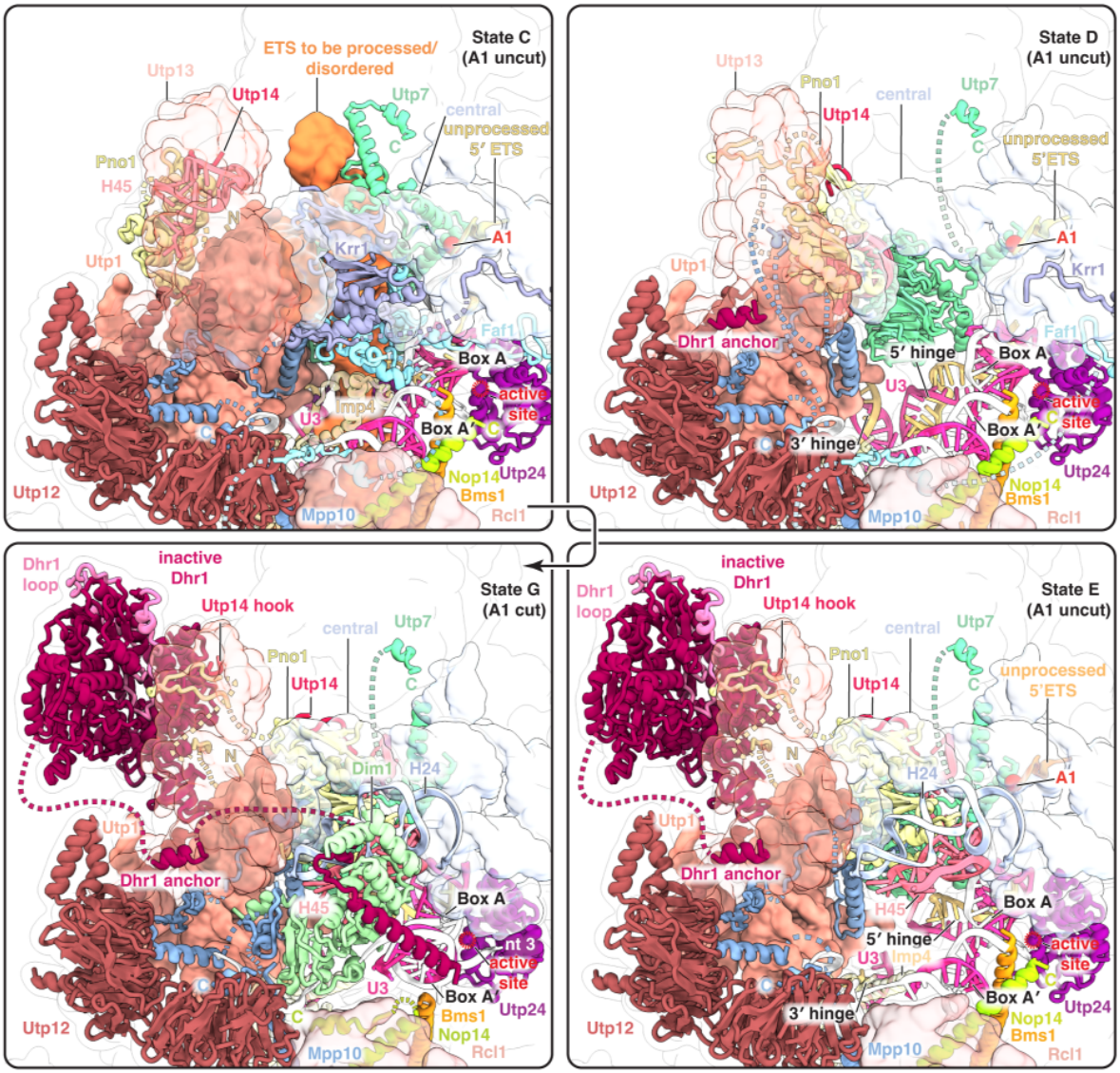

Extended Data Fig. 3. Molecular proofreading for A1 cleavage during SSU processome maturation.

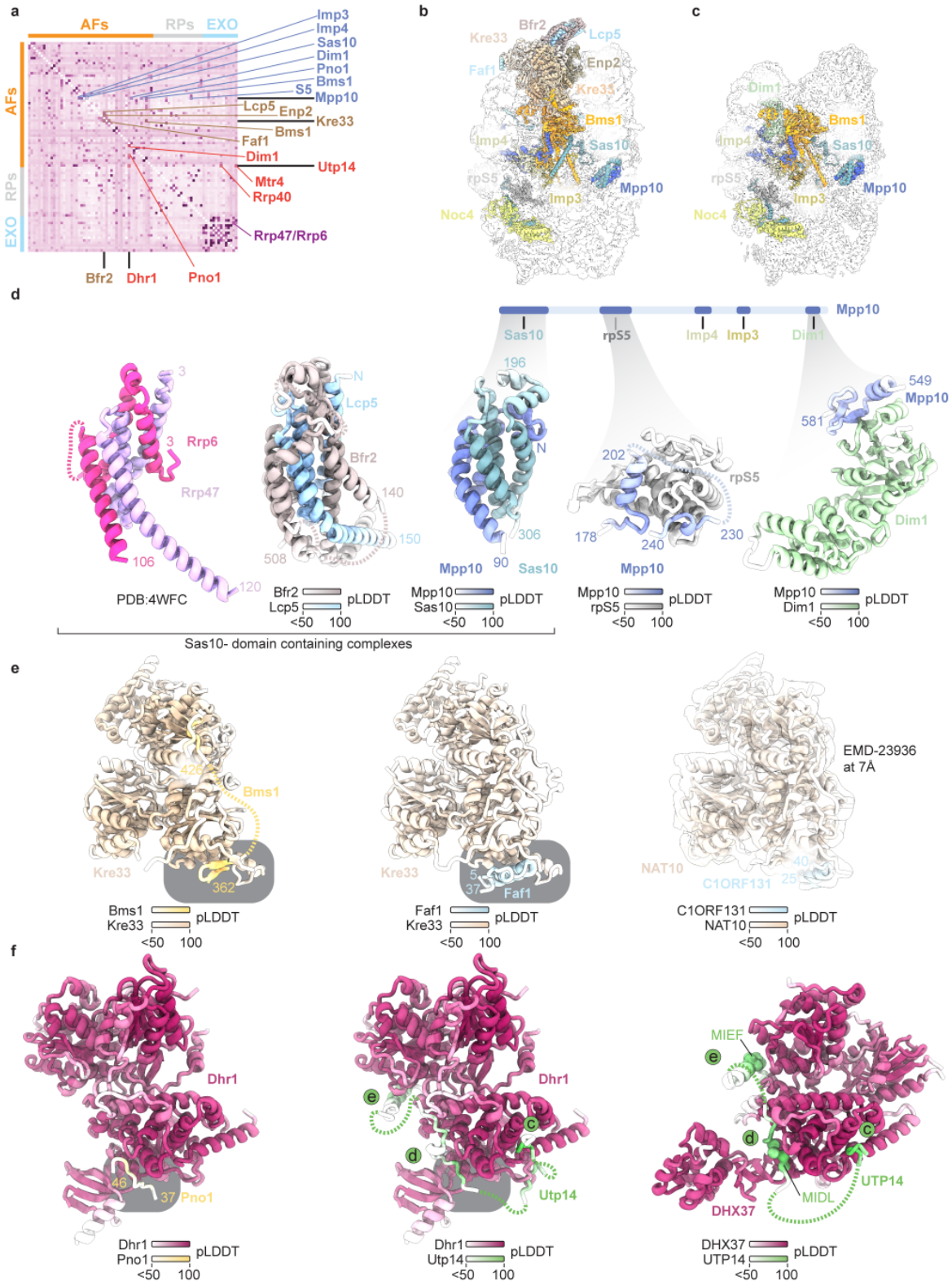

Extended Data Fig. 4. Yeast SSU processome predictome.

Plasmid Sequencing Results	Plasmid Revertants?	Amino Acid Sequencing Results ERM1:	ERM2:
Colony1:Rrp6 1-673, Utp14 ERM(1+2)^Ala	No	VMNAAAAKNG	QINKAAAAATPG
Colony1:Rrp6 1-648, Utp14 ERM(1+2)^WT	*Yes	VMNMAFMKNG	QINKGRRIYTPG
Colony2:Rrp6 1-648, Utp14 ERM(1+2)^WT	*Yes	VMNMAFMKNG	QINKGRRIYTPG

Plasmid Sequencing Results	Plasmid Revertants?	Amino Acid Sequencing Results ERM1:	ERM2:
Colony1:Rrp6 1-648, Utp14 ERM(1+2)^Ala	No	VMNAAAAKNG	QINKAAAAATPG

Extended Data Fig. 5. Yeast growth assays.

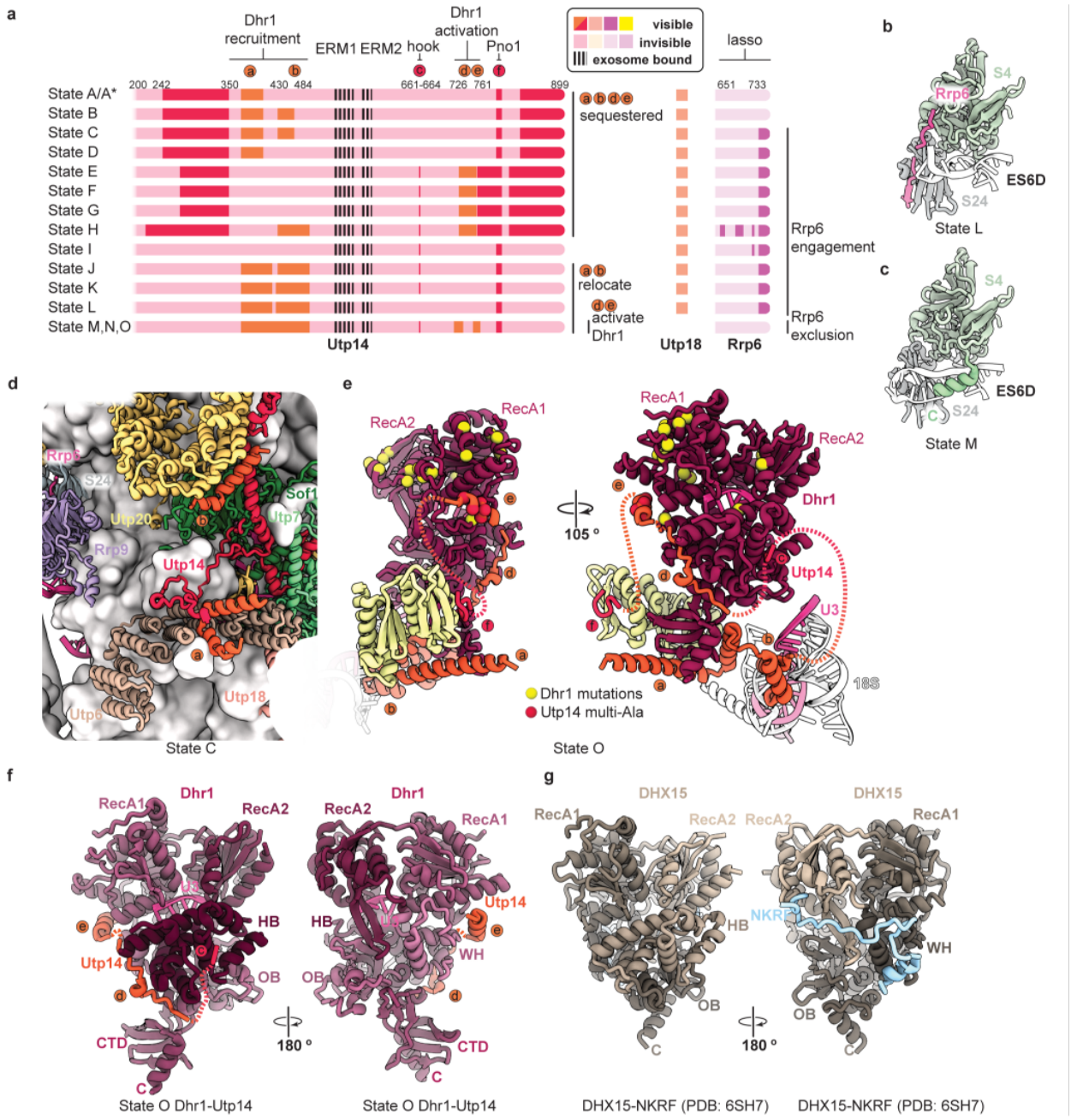

Extended Data Fig. 6. Functional elements of Utp14, Rrp6, Utp18 and Dhr1.